International Journal of Greenhouse Gas Control 66 (2017) 204–217

Contents lists available at ScienceDirect

International Journal of Greenhouse Gas Control

journal homepage: www.elsevier.com/locate/ijggc

CO_2 mineral trapping in fractured basalt

Wei Xiong[a], Rachel K. Wells[b], Anne H. Menefee[c], Philip Skemer[b], Brian R. Ellis[c], Daniel E. Giammar[a,*]

[a] Department of Energy, Environmental and Chemical Engineering, Washington University in St. Louis, St. Louis, MO 63130, United States
[b] Department of Earth & Planetary Sciences, Washington University in St. Louis, St. Louis, MO 63130, United States
[c] Department of Civil and Environmental Engineering, University of Michigan, Ann Arbor, MI 48109, United States

ARTICLE INFO

Keywords:
Geologic carbon sequestration
Fractured basalt
Siderite
X-ray μCT segmentation
Reactive transport modeling

ABSTRACT

Fractures in basalt can provide substantial surface area for reactions, and limited mass transfer in fractures can allow accumulation of cations to form carbonate minerals in geologic carbon sequestration. In this study, flood basalt and serpentinized basalt with engineered fractures were reacted in water equilibrated with 10 MPa CO_2 at 100 °C or 150 °C for up to 40 weeks. Carbonation in basalt fractures was observed as early as 6 weeks, with Mg- and Ca-bearing siderite formed in both basalts reacted at 100 °C and Mg-Fe-Ca carbonate minerals formed in the flood basalt reacted at 150 °C. X-ray μCT segmentation revealed that precipitates filled 5.4% and 15% (by volume) of the flood basalt fracture after 40 weeks of reaction at 100 °C and 150 °C, respectively. Zones of elevated carbonate abundance did not completely seal the fracture. Limited siderite clusters (< 1% volume fraction) were found in localized areas in the serpentinized basalt fracture. A 1-dimensional reactive transport model developed in CrunchTope examined how geochemical gradients drive silicate mineral dissolution and carbonate precipitation in the fracture. The model predicts that siderite will form as early as 1 day after the addition of CO_2. The predicted location of maximum siderite abundance is consistent with experimental observations, and the predicted total carbonate volumes are comparable to estimates derived from CT segmentation.

1. Introduction

Geological carbon sequestration can reduce CO_2 emissions to the atmosphere by injecting captured CO_2 into deep geologic formations (IPCC, 2005; Schrag, 2007). Most injections are in porous sedimentary rocks, which have large storage volumes but provide limited capacity to permanently capture CO_2 in the form of stable carbonate minerals (Kintisch, 2016). Basalt is a potential host rock for CO_2 sequestration because it is rich in Ca-, Mg- and Fe-bearing minerals that can react with dissolved CO_2 to form carbonate minerals, thereby trapping the injected CO_2 in stable solid phases (Gislason et al., 2010; Matter and Kelemen, 2009) A recent report on the CarbFix site in Iceland revealed that 95% of the CO_2 injected with water into basalt had been converted into carbonate minerals within 2 years (Matter et al., 2016). At the basalt pilot injection project by the Big Sky Carbon Sequestration Partnership in Washington State, carbon mineralization of injected supercritical CO_2 was also observed after two years (McGrail et al., 2017). These timescales for mineral trapping are orders of magnitude shorter than those predicted for sandstone reservoirs (Benson and Cole, 2008). Simulation studies also showed that basalt has a larger mineral trapping capacity and requires less mineral trapping time than sandstone reservoirs (Aradóttir et al., 2012; Zhang et al., 2013).

Major divalent cations necessary for carbonation reactions (e.g. Ca, Mg and Fe) are present in minerals such as olivine [$(Fe,Mg)_2SiO_4$], pyroxene [$(Na,Ca)(Mg,Fe,Al)(Al,Si)_2O_6$], and plagioclase feldspar [$NaAlSi_3O_8$-$CaAl_2Si_2O_8$] that are abundant in basalt (Oelkers et al., 2008). Olivine has the fastest dissolution rate and largest mineral trapping capacity among these minerals (Giammar et al., 2005; Oelkers et al., 2008). The injected CO_2 dissolves in water (Eq. (1)), decreases the pH (Eq. (2)), and accelerates the dissolution of the silicate minerals. The dissolution of the minerals releases divalent cations and increases the pH (Eq. (3), taking forsterite as an example), which increases the fraction of dissolved inorganic carbon present as the carbonate ion. Ultimately, carbonate minerals including calcite ($CaCO_3$), magnesite ($MgCO_3$), siderite ($FeCO_3$), and ankerite [$Ca(Fe,Mg,Mn)(CO_3)_2$] may precipitate (Eq. (4)) (Gysi and Stefansson, 2011; Kelemen and Matter, 2008; Matter et al., 2016; McGrail et al., 2017; Oelkers et al., 2008).

$$CO_{2(g)} = CO_{2(aq)} \quad (1)$$

$$CO_{2(aq)} + H_2O = CO_3^{2-} + 2H^+ \quad (2)$$

$$Mg_2SiO_{4(s)} + 4H^+ = 2Mg^{2+} + SiO_{2(aq)} + 2H_2O \quad (3)$$

* Corresponding author.
E-mail address: giammar@wustl.edu (D.E. Giammar).

http://dx.doi.org/10.1016/j.ijggc.2017.10.003
Received 20 June 2017; Received in revised form 11 October 2017; Accepted 11 October 2017
Available online 21 October 2017
1750-5836/

Table 1
Basalt compositions.

Composition	Flood basalt (FB)	Serpentinized basalt (SB)
Pyroxene	23%[a]	22%[a]
	$Ca_{0.63}Fe_{0.48}Mg_{0.83}Ti_{0.03}Al_{0.09}Si_{1.92}O_6$	$Ca_{0.83}Fe_{0.25}Mg_{0.85}Ti_{0.03}Al_{0.07}Si_{1.96}O_6$
Olivine	9%	1%
	$Mg_{1.21}Fe_{0.78}Ca_{0.01}SiO_4$	$Mg_{1.38}Fe_{0.59}Mn_{0.02}Si_{1.01}O_4$
Serpentine	1%	14%
		$Mg_{0.6}Al_{0.27}Ca_{0.11}Mn_{0.05}Fe_{1.82}Si_3O_9H_x$
Plagioclase	31%	28%
	$Ca_{0.59}Na_{0.40}Fe_{0.03}Al_{1.57}Si_{2.40}O_8$	$Ca_{0.55}Na_{0.43}Fe_{0.02}Al_{1.57}Si_{2.43}O_8$
Glass matrix and others	36%[b]	35%[c]
	$Ca_{0.04}Na_{0.33}K_{0.64}Fe_{0.01}Al_{1.06}Si_{2.93}O_8$	$Ca_{0.03}Na_{0.32}K_{0.66}Fe_{0.05}Al_{1.05}Si_{2.94}O_8$

[a] 1% is composed of orthopyroxene ($Mg_{1.34}Fe_{0.55}Ca_{0.07}Mn_{0.02}Al_{0.04}Si_{1.97}O_6$).
[b] 3% is composed of ilmenite.
[c] 3% is composed of apatite and chromite.

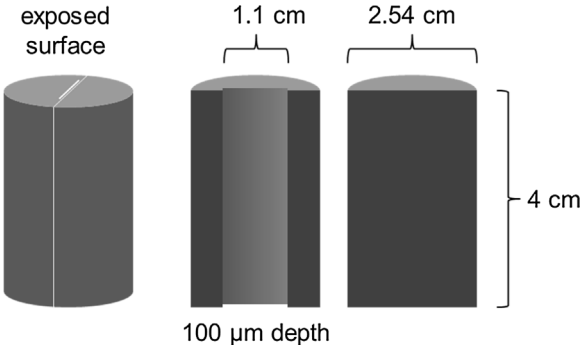

Fig. 1. Milling pattern.

$$Mg^{2+} + CO_3^{2-} = MgCO_{3(s)} \quad (4)$$

The majority of exposed reactive surfaces in basalt reservoirs are located in pores and fractures. Solute transport in such fractures can be limited to diffusion, and transport pathways may be influenced by the coupling of transport processes and geochemical reactions. Laboratory experiments have been conducted to investigate this complex relationship using both flow-through and static systems. In flow-through systems with basalt cores, permeability increased at a high flow rate but decreased for low flow rate experiments, after which secondary precipitates were observed (Luhmann et al., 2017). In another study that involved both static and flow-through systems, no observable precipitates were found in the flow-through system and siderite precipitates were identified in the static system(Adeoye et al., 2017). Sufficiently long residence times for the fluid to interact with the basalt are necessary for the fluid to become supersaturated with respect to

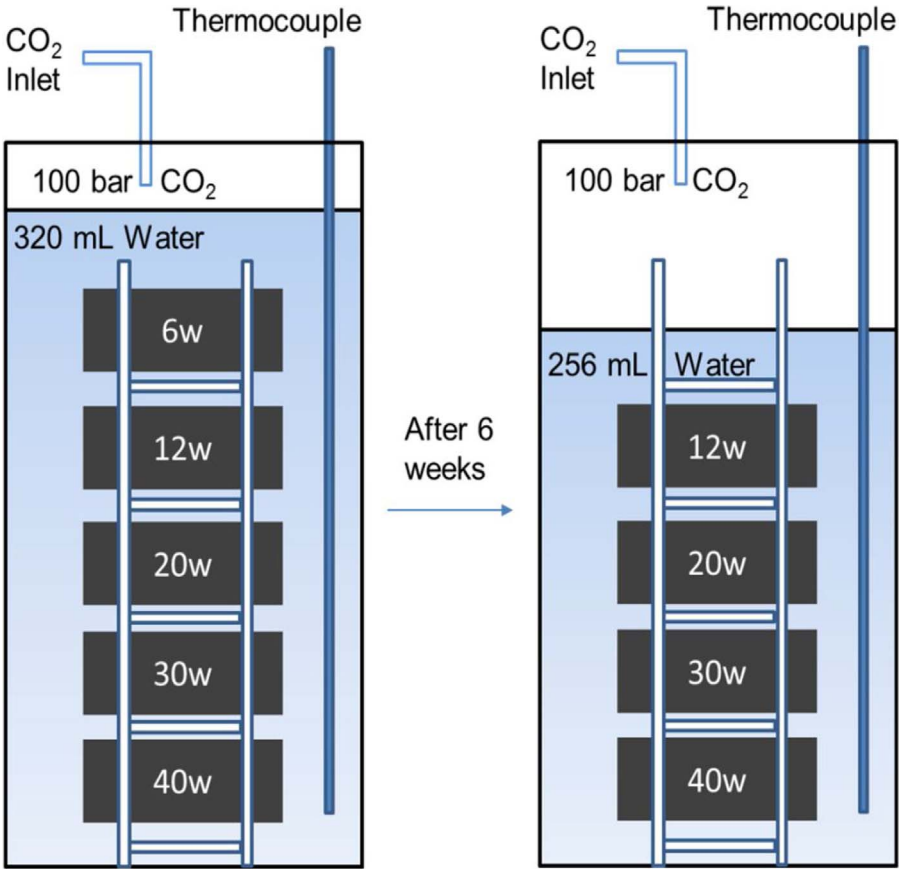

Fig. 2. Schematic diagram of experiment set up. Cores are marked 6w, 12w, 20w, 30w and 40w for their reaction time. After the designated reaction time, the core was taken out with 64 mL solution to keep the solid-to-water ratio the same (64 mL per core) for the cores that remained in the reactor.

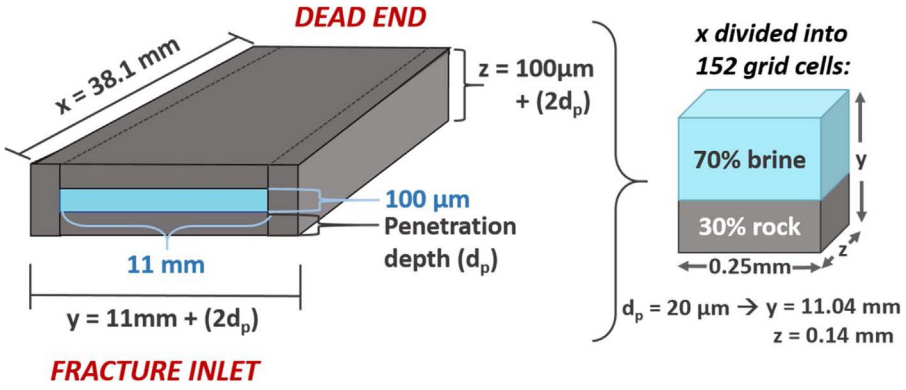

Fig. 3. Conceptual schematic of modeled domain, where the open fracture surrounded by reactive basalt surfaces is converted to an equivalent volume of porous medium discretized into 152 0.25-mm grid cells along the x-dimension parallel to the fracture surface. The fracture inlet is exposed to CO_2-acidified brine under constant pressure (10 MPa), while the dead end simulates the epoxy seals in the static experiments. The penetration depth (d_p) in the figure refers to the amount of mineral that the solution penetrated, or dissolved, during the experiments. Note that while the figure represents the domain as a 3D fracture to indicate how porosity was calculated, all models were constructed in 1D with each cell containing the pore and mineral fractions indicated in the subfigure on the right.

Table 2
Mineral abundances and specific surface areas for reactive transport modeling.

Mineral	Flood basalt		Serpentinized basalt	
	Initial volume fraction (%)	Specific surface area (m^2/g)	Initial volume fraction (%)	Specific surface area (m^2/g)
Primary minerals				
Diopside	16	0.0034	14	0.0017
Hedenbergite	6	0.0034	8	0.0017
Albite	18	0.0225	13	0.0225
Anorthite	12	0.0225	19	0.0225
Antigorite	4	0.18	0	0.18
Greenalite	11	0.18	0	0.18
Forsterite	0	–	8	0.009
Fayalite	0	–	5	0.0018
K-feldspar	33	0.019	33	0.019
Secondary Minerals				
Calcite	–	0.037[a]	–	0.037[a]
Magnesite	–	0.0662[a]	–	0.0662[a]
Siderite	–	0.105[b]	–	0.105[b]
SiO_2(am)	–	0.0225[c]	–	0.0225[c]
Gibbsite	–	19[d]	–	19[d]

[a] Pokrovsky et al. (2005).
[b] Pokrovsky and Schott (2002).
[c] Tester et al. (1994).
[d] Kaiser and Guggenberger (2003).

secondary precipitates that include the carbonate minerals that enable mineral trapping of CO_2.

The formation of carbonate minerals has the potential for divergent effects on sequestration that include (*i*) inhibition of further mineral trapping by blocking fracture apertures and (*ii*) self-acceleration of mineral trapping by creating new fractures through the volume expansion associated with replacement of silicate minerals with carbonate minerals (Kelemen and Matter, 2008). Carbonate mineral formation could also have negligible impact on transport if the minerals form uniformly in the fracture. The objectives of this study were to determine when, where, and what types of carbonate minerals form in fractures of basalt and to explore the influence of carbonation on transport and reactions in the fracture.

2. Materials and methods

2.1. Fractured basalt cores

Columbia River flood basalt (FB) from Pullman, Washington and serpentinized basalt (SB) from Valmont Butte, Colorado were purchased from Ward's Science. The compositions of the flood basalt and the serpentinized basalt are listed in Table 1 (Wells et al., 2017). The flood basalt is unaltered and contains 9% (by mass) olivine. Olivine can be weathered to serpentine, which is a hydrous magnesium iron silicate mineral (Oelkers et al., 2008). The serpentinized basalt contains serpentine instead of olivine. Multiple cylindrical cores with 2.54 cm diameter and 4.3 cm length were made from the two basalts. Each core was cut into half cylinders. A straight 11 mm wide groove was milled on one surface using a precision CNC milling machine (Roland Model MDX-40a) with a 0.5 mm diamond bur (Fig. 1). The milled half-cylinder was polished with sandpaper until the groove was 100 µm deep. The groove depth was determined by comparing the z-value of the spots on the groove and the spots on the closest polished surface in an optical microscope (ZEISS, Observer Z1). The surface of the other half cylinder was also polished. The two half cylinders were attached together to form one cylinder with the 100 µm groove in the middle. The bottom and the outer side surfaces of the cylinder were coated with epoxy (MasterBond EP42HT-2), exposing only the upper fracture opening to create a "dead-end" microfracture (Adeoye et al., 2017).

2.2. Batch experiments

Three batch experiments were conducted. In each batch, five cores were placed on a multilevel PTFE holder, which was in a PTFE liner inside of a 600 mL stainless steel high pressure vessel (Parr Instrument) (Fig. 2). Ultrapure water (320 mL in total, 64 mL per core) was added to fully immerse the cores at the beginning of the experiment. Batch reactors with FB and SB cores were heated to 100 °C and a third reactor with FB cores was heated to 150 °C. Heating was provided by heating tape (Omega, CSi32 Series). A headspace of 10 MPa CO_2 was maintained by a syringe pump (500D, Teledyne Isco). Cores were collected together with 64 mL of the bulk aqueous solution in the reactors after reacting for 6, 12, 20, 30 and 40 weeks (cores marked as 6w, 12w, 20w, 30w and 40w in Fig. 2). In this sampling method, the solid-to-water ratio was kept the same throughout the reaction. Aqueous samples were filtered using 0.2 µm PES syringe filters. Before starting each experiment, three flushing steps were performed to remove residual O_2 with 1 MPa CO_2 pumped into the reactor headspace and then immediately degassed to atmospheric pressure. The process of cooling and depressurizing for sample collection and restarting the reactor was ~5 h.

2.3. Analytical methods

The 40-week cores were scanned by X-ray computed tomography (CT) before (Scanco uCT 40, voxel resolution 15 µm) and after reaction (Zeiss Xradia Versa 520, 23.8–24.8 µm, and Nikon Metrology XTH225, 20.5 µm) to examine the precipitates formed inside the fracture without breaking the core into two parts. The reconstructed cores were exported as stacks of image slices perpendicular to the fractures. As the cores were not perfectly vertical during the scans, fractures were first aligned in ImageJ (Schneider et al., 2012) using the StackReg plugin (Thevenaz et al., 1998). The fractures were then isolated and the image stack re-sliced, resulting in a series of images parallel to the fracture from the milled surface to the smooth surface. Because each core had only 3–6

Table 3
Mineral kinetic inputs for reactive transport modeling.

Mineral	Acid mechanism			Neutral mechanism		Basic mechanism		
	log k_{25} (mol/m^2/s)	E_a (kcal/mol)	n^{H+}	log k_{25} (mol/m^2/s)	E_a (kcal/mol)	log k_{25} (mol/m^2/s)	E_a (kcal/mol)	n^{OH-}
Diopside	−6.36[e]	22.97[e]	0.71[e]	−11.11[e]	9.70[e]	–	–	–
Hedenbergite[a]	−6.36	22.97	0.71	−11.11	9.70	–	–	–
Albite[d]	−8.86[f]	16.2[f]	0.50[f]	−12[f]	15.9[f]	–	–	–
Anorthite[d]	−8.86[f]	16.2[f]	0.50[f]	−12[f]	15.9[f]	–	–	–
Antigorite	−10.01[g]	16.73[g]	0.45[g]	−12.08[h]	13.53[h]	–	–	–
Greenalite[b]	−10.01	16.73	0.45	−12.08	13.53	–	–	–
Forsterite	−6.85[e]	16.06[e]	0.47[e]	−10.64[e]	18.88[e]	–	–	–
Fayalite	−6.85[c]	22.56[e]	0.47[e]	−12.8[e]	22.56[e]	–	–	–
K-feldspar	−9.45[f]	12.41[e]	0.50[e]	−12.41[e]	9.08[e]	−21.2[e]	22.49[e]	−0.823[e]
Calcite	−0.3[e]	3.44[e]	1.0[e]	−5.81[e]	5.62[e]	–	–	–
Magnesite	−6.38[e]	3.44[e]	1.0[e]	−9.34[e]	5.62[e]	–	–	–
Siderite	−3.74[i]	13.38[i]	0.90[i]	−8.90[f]	15.0[f]	–	–	–
SiO_2(am)	–	–	–	−9.7[j]	18.88[j]	–	–	–
Gibbsite	−7.65[e]	11.35[e]	0.992[e]	−11.5[e]	14.63[e]	−16.65[e]	19.14[e]	−0.784[e]

[a] Hedenbergite kinetics set to those of diopside (Palandri and Kharaka, 2004).
[b] Greenalite kinetics set to those of antigorite (Orlando et al., 2011; Teir et al., 2007).
[c] Fayalite reaction rate set to that of forsterite in calibrating experimental effluent data.
[d] Albite and antigorite kinetics were set to those of labradorite, consistent with the plagioclase composition of both samples.
[e] Palandri and Kharaka (2004).
[f] Knauss et al. (2005).
[g] Teir et al. (2007).
[h] Orlando et al. (2011).
[i] Golubev et al. (2009).
[j] Carroll et al. (2013).

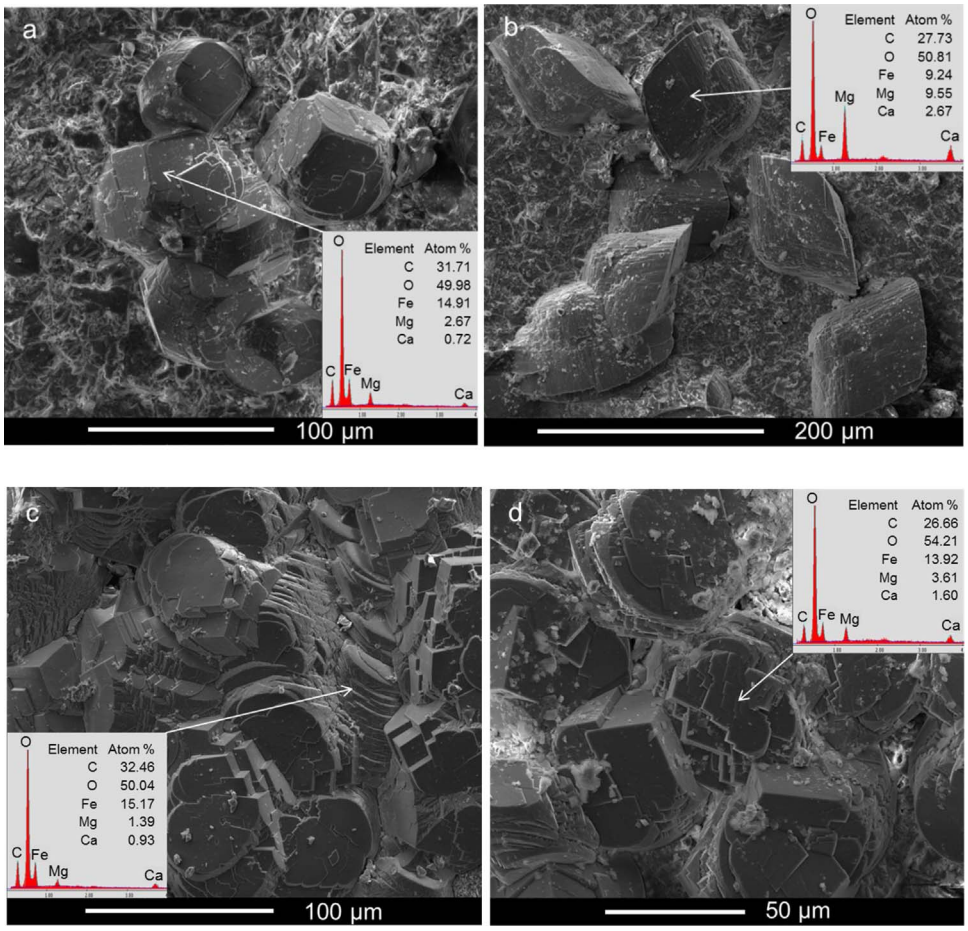

Fig. 4. Carbonate minerals formed in the milled fracture surfaces of flood basalt after reactions for 40 weeks with a) a siderite precipitate formed at 100 °C in water equilbrated with 10 MPa CO_2, b) Fe-Mg-Ca carbonate formed at 150 °C in water equilibrated with 10 MPa CO_2, c) siderite cluster in serpentinized basalt reacted at 100 °C in water equilbrated with 10 MPa CO_2 for 40 weeks and d) a siderite precpitate in flood basalt reacted at 100 °C in water equilbrated with 10 MPa CO_2 for 20 weeks.

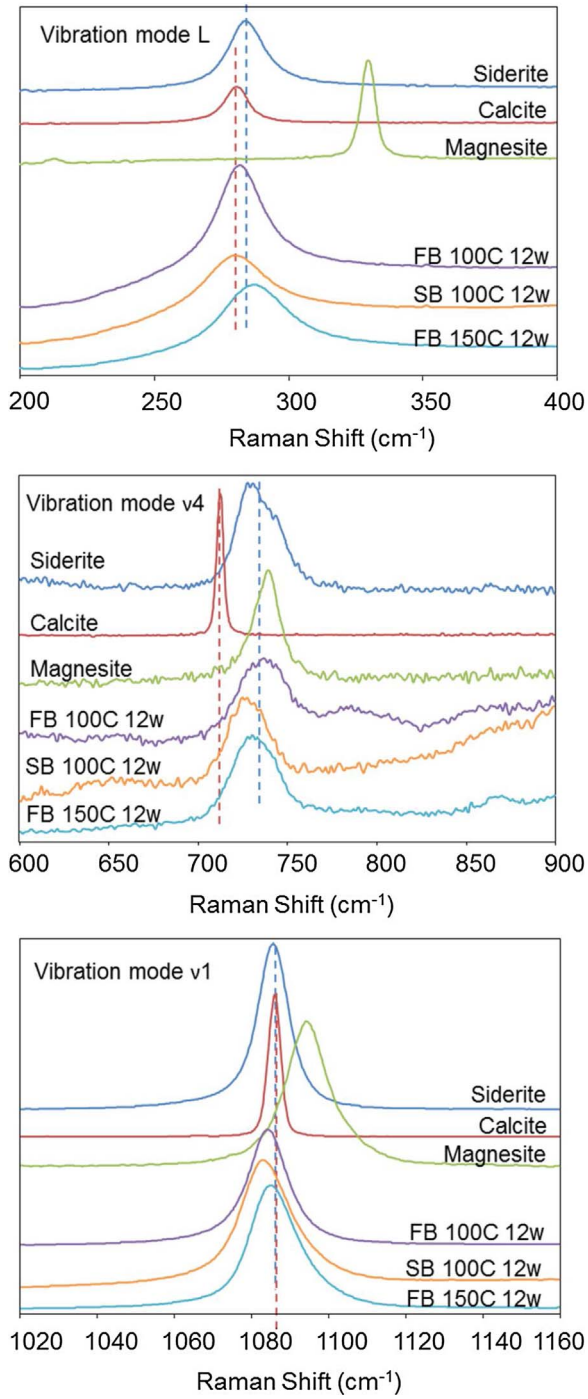

Fig. 5. Comparison of Raman spectra of precipitates on flood basalt reacted at 100 °C and 150 °C and serpentinized basalt reacted at 100 °C with siderite, calcite and magnesite standards. Raman peaks in the range of a) 200–400 cm^{-1}; b) 600–900 cm^{-1}; c) 1020–1160 cm^{-1}.

fracture images depending on the voxel resolution of the scan and the contrast often differed significantly between the fracture surfaces and interior, each image was segmented separately for optimal resolution. Images were pre-processed in ImageJ to remove regions of epoxy that were not considered as available fracture volume for precipitation. Thresholding was performed in Ilastik, an interactive software that uses specified feature sizes and descriptors (e.g. intensity or texture) to classify pixels and then segments classes by minimizing the cut between foreground and background seeds. Manual seeding trains the software to identify user-defined pixel classes, which are then segmented by optimizing the minimal cut between foreground and background seeds based on weighted combinations of intensity and edge filters (Sommer et al., 2011). Here, pixels were classified as precipitate or fracture, and resulting binary images were exported for quantification. Precipitate volumes and fractions relative to the total fracture volume were then calculated in Matlab for each core based on the voxel resolutions of the scans. To compare spatial distributions of the segmentations with the point counting results along the fracture surfaces, precipitate volumes were also calculated over 5-mm intervals from the fracture inlet to the sealed end. It should be noted that this approach failed to capture the precipitates at the base of the FB-150C core due to inconsistent contrast, but overall it provides a reasonable estimate of precipitate volumes within the data quality and resolution of the CT images.

After CT scanning of intact cores was performed, the two half cylinders were separated. Optical microscopy (LEICA, DFC295) was used to detect precipitates along the milled surface. Raman spectra of observable precipitates were collected with a laser Raman microprobe using a 532 nm laser (HoloLab Series 5000, Kaiser Optical). The precipitate morphology and elemental composition were examined by scanning electron microscopy and energy dispersive X-ray spectroscopy (FEI Nova 230). The precipitate distribution on the groove was assessed by CT segmentation of the precipitate volume in each 5 mm increment from inlet to outlet and also by a point counting station (LEICA, DM2700p) with a 10× objective. The point counting was conducted by moving a 100 µm square field of view step-by-step horizontally across the 11-mm wide fracture (110 steps) at certain fracture depths and counting the number of squares that contained a precipitate regardless of precipitate size or abundance. The carbonate point count percentage at each depth is the percentage of the number of squares with carbonate in them divided by the total squares counted. Aqueous samples were analyzed by inductively coupled plasma mass spectrometry (Perkin Elmer, Elan DRC II) and ion chromatography (Theromo Scientific, DIONEX ICS-1600).

2.4. Reactive transport modeling

To understand how geochemical gradients drive precipitation patterns observed inside the fractures, 1D reactive transport models were developed in CrunchTope (Steefel et al., 2015) using the EQ3/EQ6 thermodynamic database. The geochemical gradients are generated by the pH-dependent dissolution of minerals in the basalt and the diffusion of inorganic carbon into the fracture together with the diffusion of solutes out of the fracture. Because the code is designed for porous media, the system consisting of an open fracture surrounded by reactive mineral was modeled as an equivalent porous medium with dimensions and water:rock ratios calculated from the geometry in Fig. 3. Based on observations from pre- and post-reaction CT scans of these core samples, it was assumed that the reactive fluid could penetrate, or interact with, the surrounding rock to a depth of 20 µm on all sides of the fracture over the 40-week experiments. This corresponded to an initial porosity of 30% (i.e. mineral fraction of 70%) and water:rock ratio of 2.5. Although transport is only considered in one dimension along the length of the fracture, which was discretized into 152 grid cells (0.25 mm in length), each cell was also assigned a width (11.04 mm) and height (0.14 mm) to capture the total volume of rock and fluid in the model domain illustrated in Fig. 3. Specifying y- and z-dimensions was also necessary because the code solves 1D problems by integrating over a volume via the finite difference method at each time step.

To match experimental conditions in the batch reactors, a constant pressure boundary, consisting of pure water equilibrated with CO_2 at 10 MPa and the experimental temperature (100 °C or 150 °C), was imposed at the inlet. CO_2 fugacity was calculated directly in the code (Duan and Sun, 2003). While cations are allowed to diffuse back through the inlet as concentration gradients develop, the models do not allow for feedback between the fracture and bulk solution. Results for models where the inlet composition was set to that of the actual bulk

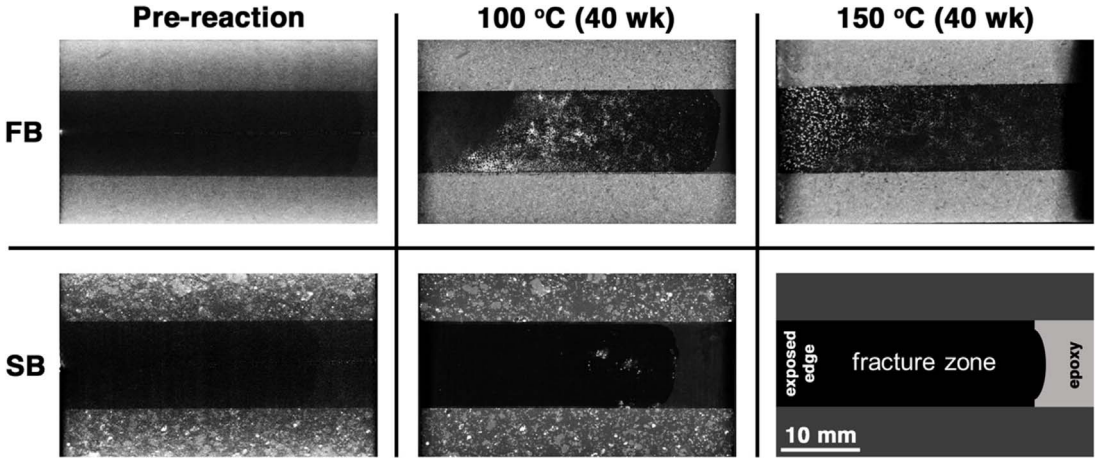

Fig. 6. X-ray CT images of fracture cross section in flood and serpentinized basalt cores reacting in 100 °C or 150 °C for 40 weeks. Schematic of fracture orientation is shown in bottom right. Dark zone is the fracture. Left end is the fracture inlet that exposed to the bulk solution. Right end is sealed with epoxy. The white dots along the fracture are carbonate precipitates.

solution measured at experimental sampling points differed negligibly from those where the inlet boundary was maintained as pure water, indicating the influence of the bulk solution was insignificant relative to cation accumulation within the fracture. A no-flux boundary was set at the bottom of the fracture to mimic the sealed end of the core. Diffusion was the only transport mechanism considered (i.e., no advective or dispersive fluxes were permitted across the inlet boundary) with fixed diffusion coefficients of 7.5×10^{-9} m^2/s (100 °C) or 12.33×10^{-9} m^2/s (150 °C) applied for all species (Cadogan et al., 2014). Because diffusion-limited transport does not consider permeability in the code, this was not included as a model input.

The primary mineralogy of the serpentinized and flood basalt samples was set based on previous calibrations (Menefee et al., 2017), whereby effluent data from flow-through experiments using the same cores and experimental conditions were matched to model outputs by adjusting mineral volume fractions within a few percent of wavelength-dispersive spectroscopy (WDS)-derived compositions (Adeoye et al., 2017). Because the effluent chemistry data used as a benchmark in the previous calibration are sensitive to heterogeneities along fracture pathways and inter-sample variation, some mineral abundances were adjusted from the previously calibrated values to be more consistent with the WDS analysis. For the flood basalt, 36% of the pyroxene, which was all designated as diopside in prior models, was set to hedenbergite to account for the appreciable Fe content of the pyroxene ($Ca_{0.63}Fe_{0.48}Mg_{0.83}Ti_{0.03}Al_{0.09}Si_{1.92}O_6$). Additionally, a higher percentage of forsterite was included to match the Mg:Fe composition of the olivine ($Mg_{1.21}Fe_{0.78}Ca_{0.01}SiO_4$), and the 1% of serpentine present in the samples was neglected. For the serpentinized basalt, olivine (1%) was neglected while serpentine was modeled with an 11:4 ratio of greenalite:antigorite to match the Fe:Mg ratio in the serpentine of the actual samples ($Mg_{0.6}Al_{0.27}Ca_{0.11}Mn_{0.05}Fe_{1.82}Si_3O_9H_x$). Primary mineral specific surface area (SSA) values for each core sample were applied directly from the previous calibration, where primary mineral SSAs were fine-tuned to simulate experimental effluent data. The FB values, which had been calibrated to a flow-through experiment at 100 °C, were also used in the 150 °C model given the lack of an experimental benchmark for conducting a separate calibration.

Based on experimental observations, calcite, magnesite, siderite, amorphous silica, and gibbsite were included as potential precipitates. All secondary minerals are assigned an initial volume fraction of 0 and threshold mineral volume fraction of 10^{-6}. The bulk surface area of secondary minerals is calculated from this threshold volume fraction until it is exceeded, at which point precipitation begins and the volume fraction is updated at each time step according to user-defined SSAs. Here, literature-reported BET specific surface areas were selected for all secondary minerals. Porosity is updated at each time step in the code based on changes in primary and secondary mineral volume fractions. Initial primary and secondary mineral volume fractions and SSAs selected for each basalt core are summarized in Table 2.

Mineral dissolution and precipitation are assumed to proceed reversibly according to the transition state theory. In the absence of adequate precipitation kinetic data, literature-reported dissolution rates are applied to both processes. To maintain flexibility, reaction rates are calculated directly in the code for a given temperature using the Arrhenius relationship:

$$k = k_{25} \exp\left[\frac{-E_a}{R}\left(\frac{1}{T} - \frac{1}{298.15}\right)\right]$$

The reaction rate at 25 °C (k_{25}) and activation energy (E_a) for each mineral were taken from literature where available (Table 3). Parallel rate laws are used to account for reaction pH dependence, where constants for the exponential dependence of a rate on H^+ (acid mechanism) or OH^- (basic mechanism) were also taken from literature. Due to a lack of data for Fe-rich serpentine, greenalite was assigned the same kinetic parameters as antigorite. Other than fayalite, where k_{25} was set to that of forsterite in our previous study to match effluent Fe data, reported reaction rates were applied directly. This simplification may underestimate overall olivine dissolution but olivine is still the most reactive primary mineral phase.

3. Results

Mg- and Ca-bearing siderite (Fig. 4) was observed in the fractures of the flood basalt (FB) and serpentinized basalt (SB) after reacting in water equilibrated with 10 MPa CO_2 at 100 °C as early as 6 weeks. Raman spectra of the precipitates have diagnostic peaks for siderite (Fig. 5). For the flood basalt, siderite formed on the surface of the basalt fracture. Typical precipitate sizes increased from 20 μm at 6 weeks to ~100 μm at 40 weeks. For serpentinized basalt, siderite formed in larger mm-scale clusters with individual crystals growing in different orientations (Fig. 4c). The clusters tended to occur on red-colored areas that are probably large serpentine or pyroxene grains covered by iron oxides (Fig. S1). A small amount of amorphous silica also formed. For flood basalt reacted at 150 °C, a carbonate solid formed with similar amounts of Fe and Mg and less Ca per SEM-EDX (Fig. 4b). The richer Mg-content of this carbonate shifted the Raman peaks to higher frequency than those of the Fe-rich siderite formed at 100 °C (Fig. 5) (Boulard et al., 2012), and the precipitates were 100–200 μm after 40 weeks. Previous long-term static experiments with flood basalts also showed significant differences in precipitate compositions and morphologies for different basalt materials (Schaef et al., 2010).

Carbonate minerals were unevenly distributed along the flood

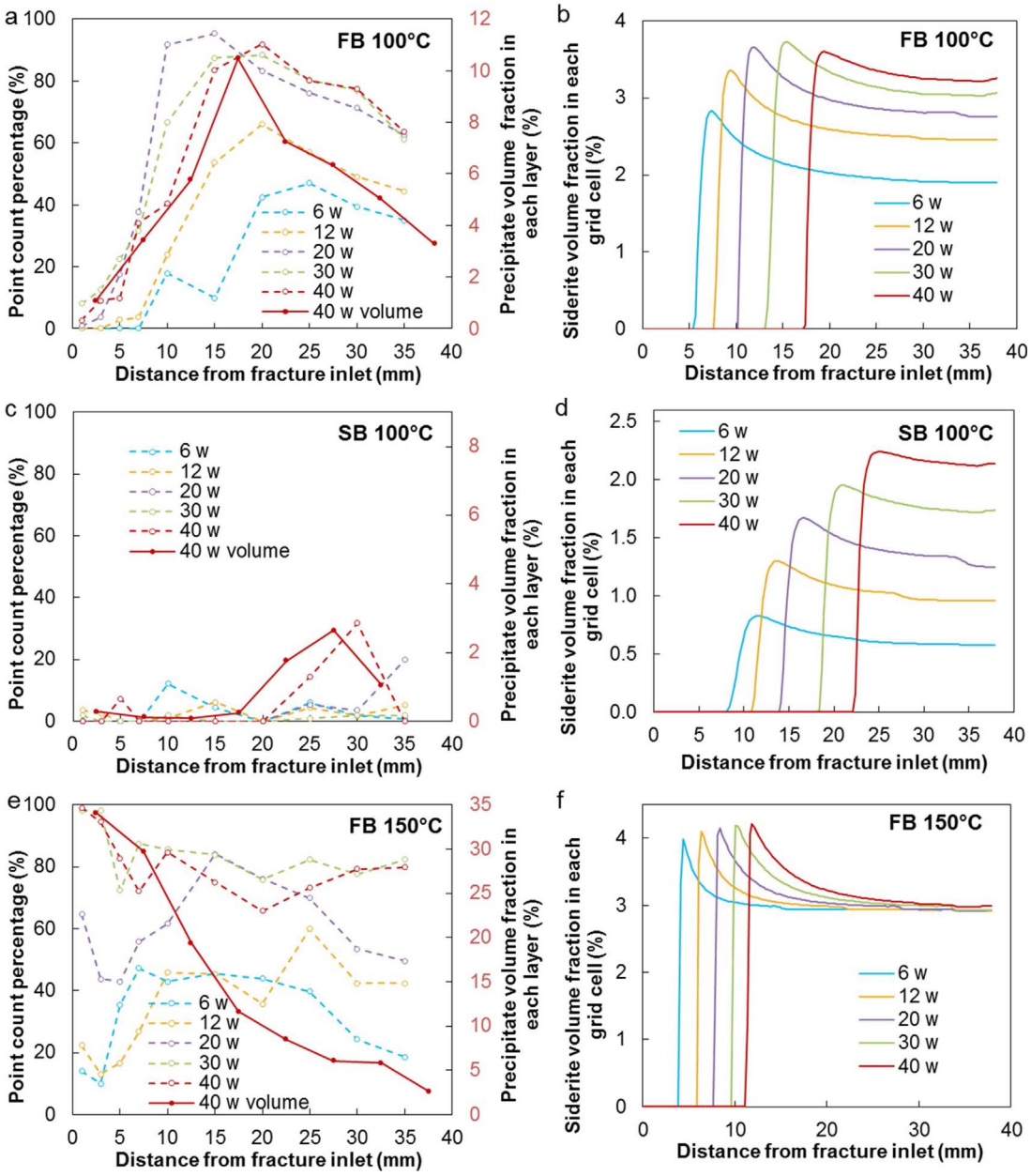

Fig. 7. a), c) and e) CT segmentation of precipitate volume fraction (solid red points and line and right axis) in each 5-mm long layer along the fracture in the flood basalt (FB) and serpentinized basalt (SB) sample and precipitate point count percentage (open symbols connected with dotted lines and left axis) on the fracture surface. The point count percentage represents the occurrence of carbonates at 110 different locations across the fracture surface at a given distance from the fracture inlet. b), d) and f) Predicted siderite volume fraction in each grid cell of the fracture domain of basalt in reactive transport modeling. (For interpretation of the references to color in this figure legend, the reader is referred to the web version of this article.)

basalt fracture as observed using CT imaging (Fig. 6). To quantify carbonate distribution, the carbonate precipitate volume in every 5 mm layer from the fracture inlet to the sealed end was estimated by CT segmentation (Fig. 7a, c, e, solid line). For flood basalt reacted at 100 °C, limited siderite formed near the fracture inlet. The amount of siderite reached a maximum around 10–25 mm from the fracture inlet and then decreased toward the bottom of the fracture. Some carbonate precipitates were large enough to bridge the 100-μm fracture. For flood basalt reacted at 150 °C, most carbonate precipitates formed at distances 10 mm or more from the fracture inlet. Individual carbonate precipitates in this zone were ~200 μm. As observed with optical microscopy, carbonate minerals precipitated on almost the entire fracture surface (Fig. S2c) after 30–40 weeks of reaction. Many smaller carbonate minerals (~20 μm), which were below scan resolution and thus could not be captured by CT, were observed in the region 3 mm from the fracture inlet (Fig. S3). The formation of small carbonate precipitates may have been affected by the cooling and degassing process during sample collection. Larger carbonate precipitates are probably more representative of the carbonate minerals that formed during the cumulative reaction time.

In serpentinized basalt reacted at 100 °C, siderite minerals formed in mm-scale clusters at locations deeper in the fracture zone (Fig. 6). The porphyritic serpentinized basalt contains mm-scale mineral grains. Zones near large pyroxene and serpentine grains might have created localized supersaturated environments for precipitation. Despite forming in larger clusters, much less siderite formed in serpentinized basalt (Fig. 7c) than in the flood basalt reacted at 100 °C (Fig. 7a).

The spatial distribution of carbonate minerals was also analyzed by point counting. The point count percentages indicate precipitate presence regardless of size at specific depths within the fracture (Fig. 7a, c,

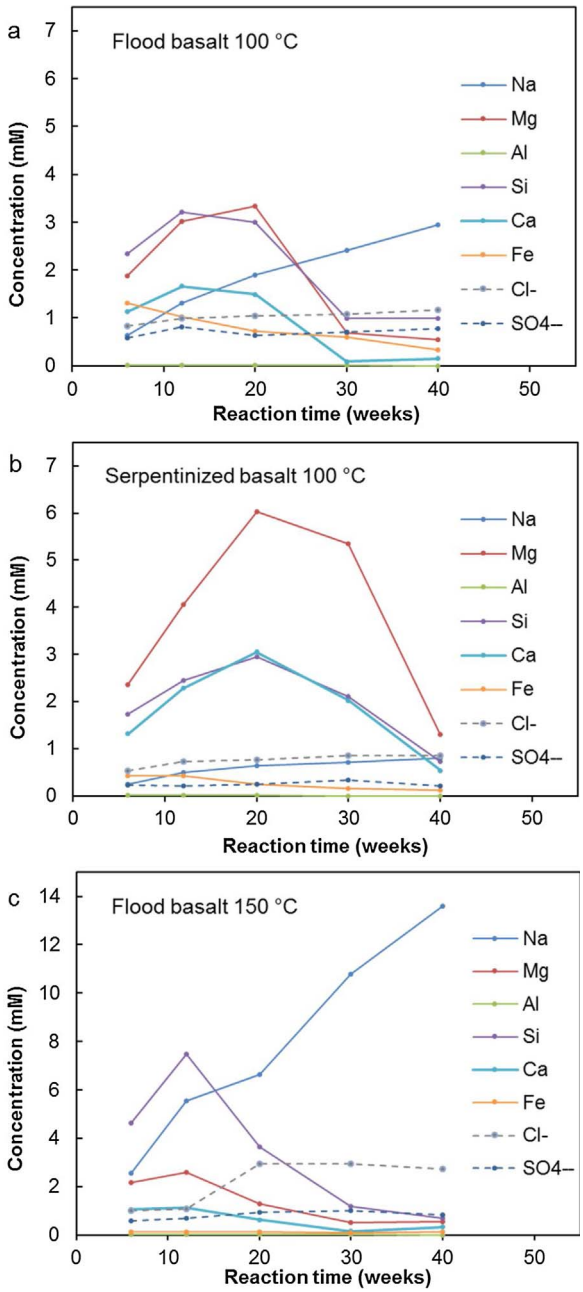

Fig. 8. Dissolved cations, $SiO_{2(aq)}$, Cl^- and SO_4^{2-} in the bulk solution of experiments with a) flood basalt reacted at 100 °C; b) serpentinized basalt reacted in 100 °C; c) flood basalt reacted at 150 °C.

e, dashed line). For flood basalt reacted at 100 °C (Fig. 7a), total occurrence of siderite in the fracture increased with longer reaction time while the location of its maximum abundance moved towards the fracture inlet, indicating that siderite built up from the fracture interior. Trends in carbonate mineral percentages based on point counting are generally consistent with CT segmentation, but the point counts indicate appreciable presence of precipitates at deeper parts of the fracture not captured in the segmentation because they were too small to be resolved by CT, especially for the flood basalt reacted at 150 °C (Fig. 7e).

Major species concentrations in the bulk solution were shown in Fig. 8 for the three batches. Overall for divalent cations, Mg^{2+} had the highest concentration, followed by Ca^{2+} and Fe^{2+} for all reaction times. The divalent cations increased with reaction time, reached a maximum, and decreased as reaction went on. This indicated precipitation involving these divalent cations was triggered after a certain amount of reaction time.

4. Discussion

4.1. Carbonate mineral formation

In this study the observed precipitation of siderite in the flood basalt fracture was expected and consistent with modeling results and measured bulk fluid compositions. The precipitates observed were carbonate solids dominated by Fe with Mg and Ca substitutions (Fig. 4). The reactive transport model predicts carbonate mineral formation as early as 1 day and indicates that siderite is the most thermodynamically favorable carbonate mineral in the basalt after 40 weeks of reaction (Table 4). The model can only predict pure carbonate mineral endmembers, which is a limitation when compared to experimental results where carbonate minerals contain cation substitutions. Although magnesite is predicted to be supersaturated in the fracture at early time steps (Fig. 9), little is predicted to form because its reaction rate is about 4 orders of magnitude below those of calcite and siderite under these conditions. Consequently, most dissolved Mg^{2+} diffuses out of the fracture due to the concentration gradient. In reality this Mg^{2+} could be taken up by favorable secondary phases, as observed experimentally in the mixed carbonates.

Although siderite has been predicted to form in basalt (Luhmann et al., 2017; Snæbjörnsdóttir et al., 2017), it has rarely been observed in field and laboratory experiments (Luhmann et al., 2017; Pollyea and Rimstidt, 2017; Snæbjörnsdóttir et al., 2017). In the CarbFix project, calcite formed under site conditions of 20–30 °C and alkaline pH of 8.4–9.4 (Matter et al., 2016). Other carbonate minerals such as ankerite, siderite and mixed Ca-Mg-Fe carbonates were not observed at the site, although they were supersaturated in the monitoring fluids (Snæbjörnsdóttir et al., 2017). In the Big Sky CO_2 injection into the Columbia River Basalt (CRB), ankerite nodules [$Ca(Fe,Mg,Mn)(CO_3)_2$] precipitated in the basalt pores at the site conditions of 7.7 MPa and 36–44 °C (McGrail et al., 2017). In a laboratory study in which similar CRB samples were reacted in CO_2-rich water for 180 days, calcite was identified at 12–25.5 MPa and 55–116 °C, while kutnohorite [$Ca(Mn,Ca)(CO_3)_2$] formed at 31 MPa and 137 °C (Schaef et al., 2011). An experimental study with Icelandic basaltic glass found that the main carbonation products were dolomite-ankerite solid solutions for reactions below 100 °C and that calcite became dominant for reactions above 150 °C (Gysi and Stefansson, 2012). Another study with mid-ocean ridge basalt provided evidence that Fe-bearing magnesite formed at 150 °C and 28 MPa CO_2 (Sissmann et al., 2014). In our previous study with powder packed beds of the same flood basalt from which the cores in this study were prepared, Mg- and Ca-bearing siderite was observed at 100 °C, 10 MPa CO_2 within 4 weeks (Xiong et al., 2017). Carbonation products can vary in basalt with different compositions and reaction conditions including pH, temperature and saturation status.

4.2. Indications from bulk solution chemistry

In the experiment, the bulk solution chemistry provides information on basalt dissolution from the outer surface of the cores and from any diffusion of solutes out of the fracture. After 40 weeks of reaction the most abundant divalent cation in the bulk solution was Mg^{2+} followed by Ca^{2+} and Fe^{2+} (Fig. 8), which is consistent with the order of dissolved cation concentrations in the fracture predicted by the models (Fig. 10). The solubility product of siderite is two orders of magnitude smaller than those of magnesite and calcite (Table S1). At the experimental conditions, siderite has the highest calculated saturation indices in the bulk solution (Fig. 11), followed by magnesite and calcite. The calculated pH is 3.2 initially and rises to 4 ~ 5 after reaction both in the bulk solution based on measurements (Fig. 11d) and in the fracture based on the reactive transport model (Fig. 12). In this low pH range

Table 4
Estimated carbonate mineral volume in the 100 μm fracture of the cores reacted for 40 weeks.

Reaction time	6 weeks	12 weeks	20 weeks	30 weeks	40 weeks
FB 100C					
Model prediction of precipitate volume in the fracture domain (mm^3)					
total calcite	0.27	0.38	0.25	0.00	0.00
total magnesite	1.99×10^{-4}	2.64×10^{-4}	2.63×10^{-4}	2.29×10^{-4}	1.89×10^{-4}
total siderite	1.01	1.24	1.26	1.21	1.04
Total carbonate	1.28	1.62	1.51	1.21	1.04
CT segmentation of precipitates volume in the fracture (mm^3)					1.73
CT segmentation of precipitate volume fraction[a]					5.43%
SB 100C					
Model prediction of precipitate volume in the fracture domain (mm^3)					
total calcite	0.58	0.63	0.26	0	0
total magnesite	0.00	0.00	0.00	7.00×10^{-5}	3.86×10^{-5}
total siderite	0.29	0.43	0.51	0.53	0.51
Total carbonate	0.86	1.06	0.77	0.53	0.51
CT segmentation of precipitates volume in the fracture (mm^3)					0.39
CT segmentation of precipitate volume fraction[a]					0.88%
FB 150C					
Model prediction of precipitate volume in the fracture domain (mm^3)					
total calcite	1.71	1.51	1.28	0.99	0.70
total magnesite	1.53	1.49	1.42	1.34	1.25
total siderite	1.61	1.56	1.51	1.46	1.42
Total carbonate	4.86	4.56	4.21	3.79	3.37
CT segmentation of precipitates volume in the fracture (mm^3)					7.09
CT segmentation of precipitate volume fraction[a]					14.75%

[a] Percentage of the total initial fracture volume that becomes filled with carbonates.

and with the measured concentrations of Fe^{2+}, Mg^{2+}, and Ca^{2+}, siderite is thermodynamically favorable relative to calcite and magnesite.

4.3. Uneven distribution of precipitates

The spatial distribution of carbonate precipitation is a result of opposing chemical gradients along the diffusion-limited dead-end fracture as demonstrated in the reactive transport modeling. As dissolved CO_2 diffuses into the fracture, the concentration of dissolved inorganic carbon initially decreases with distance into the fracture and becomes more uniform with increasing reaction time (Fig. 13). At the fracture inlet, the pH is low (Fig. 12). Cation concentrations at the fracture inlet are as small as in the bulk solution (Giammar et al., 2014). The distribution of divalent cations along the length of the fracture (Fig. 10) is determined by the interactions of dissolution-precipitation reactions and diffusive transport of cations released from the fracture walls towards the bulk solution due to concentration gradients.

Although certain locations were filled with more carbonate precipitates than others, the transport pathways into the deeper fracture zone were not blocked, even over the longest experiments performed as part of this study (40 weeks). Carbonates were continuing to form in the fracture below the location where most carbonate precipitates had formed. For flood basalt reacted at 100 °C for 40 weeks, the largest siderite abundance appeared 15–20 mm from the fracture inlet (Fig. 7a). Based on CT segmentation, carbonates occupied roughly 10.5% of the available 100-μm fracture volume in this 5-mm long region. Even in the maximum precipitation zone, there was sufficient space for solutes to diffuse through the fluid in the fracture. Our previous study with olivine packed beds and olivine aggregates also demonstrated that extensive carbonate mineral formation in certain locations would not entirely block mass transfer to and reaction in deeper unreacted zones (Wells et al., 2017; Xiong and Giammar, 2014). Blockage due to precipitation was not observed with powder packed beds of the same flood basalt and serpentinized basalt as in this study (Xiong et al., 2017).

4.4. Comparison with modeling results

Model predictions of total carbonate volumes (Table 4) were consistent with those determined by CT segmentation, while predicted spatial distributions of siderite were similar to those observed experimentally and quantified via point counting (Fig. 7a, c, e). The predicted siderite formation along the fracture (Fig. 7b, d, f) follows similar spatial distribution trends as observed in the experiment. Only a limited amount of carbonates including siderite formed near the fracture inlet due to the low pH and lack of divalent cation accumulation. In the flood basalt reacted at 100 °C, the predicted amount of siderite increases sharply below the dissolution-only region and siderite reaches a maximum around 10–20 mm from the fracture inlet, roughly coinciding with the predicted location of the maximum amount of dissolved Fe^{2+} in the fracture (Fig. 10). Locations of maximum divalent cation concentrations in the fracture, which result from diffusion into and out of the fracture due to CO_2 intrusion and concentration gradients, respectively, were often indicative of maximum carbonate precipitation, indicating that cation concentrations are the most important factor affecting the locations of carbonate precipitation. The predicted maximum extent of carbonate precipitation occurred near the inlet (< 10 mm into the fracture) of the flood basalt at 150 °C (Fig. 7f). For serpentinized basalt reacted at 100 °C, experimentally most siderite formed deeper in the fracture (Fig. 7c). The predicted maximum siderite location (25 mm into the fracture) in a serpentinized basalt core after 40 weeks of reaction (Fig. 7d) was consistent with that experimental observation. Other potential secondary precipitates such as amorphous silica and gibbsite were also predicted by the model (Figs. S4–S6). However, we only identified iron-rich carbonate as the predominant secondary precipitates in the experiment using the characterization methods in this study.

A divergence of the current 1-dimensional model predictions from experimental observations is that carbonates are predicted to precipitate and then later dissolve at specific locations near the fracture inlet (Fig. 7b), while experimental observations indicate that carbonate mineral abundance in the fracture continued to increase at all locations until 20–30 weeks of reaction and became almost stable after 40 weeks with no observable evidence of re-dissolution (Fig. 7a). The re-

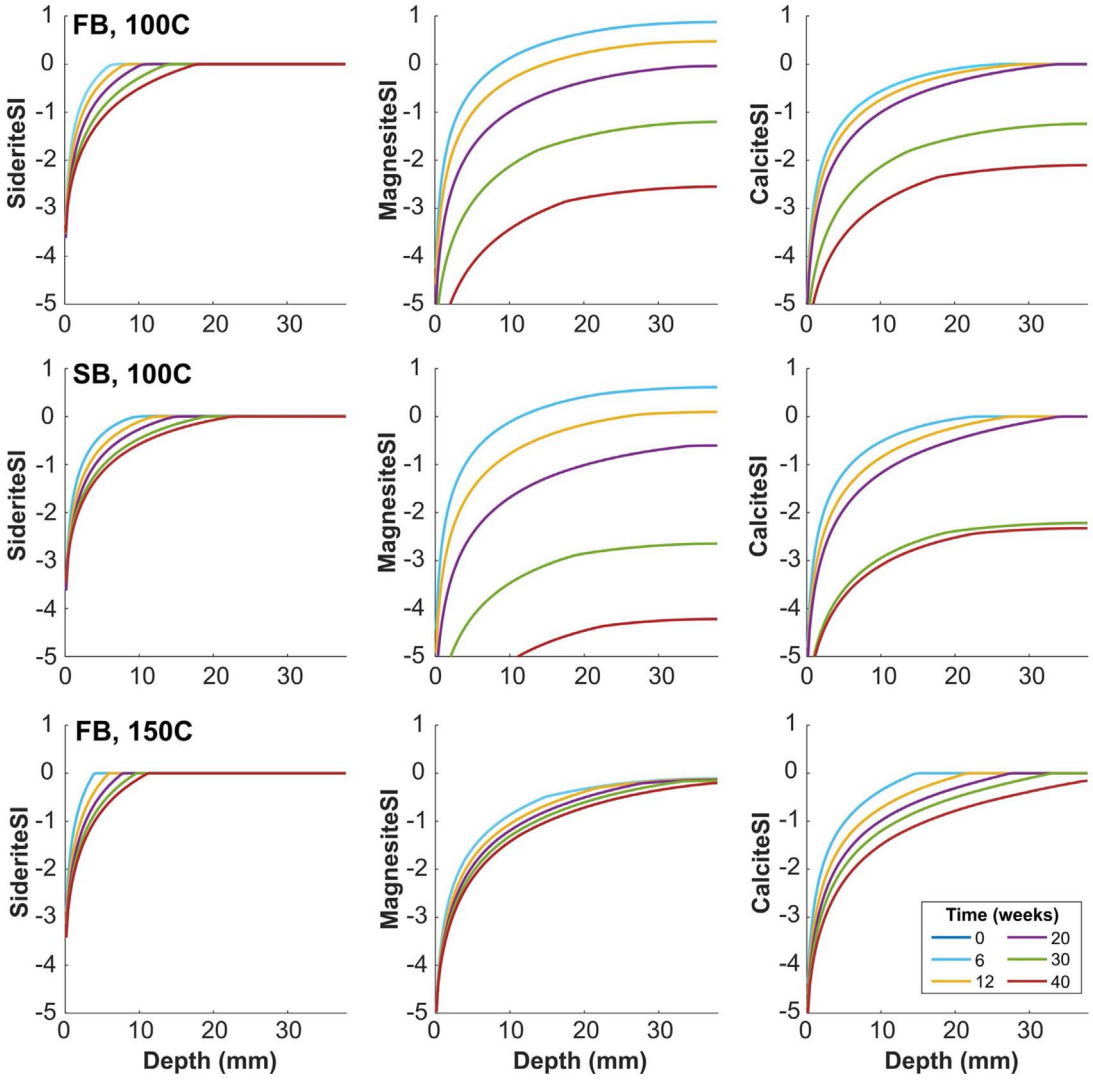

Fig. 9. Saturation indices of magnesite, calcite and siderite predicted by the model. Magnesite is supersaturated in some cases but is not allowed to precipitate because its precipitation is expected to be kinetically hindered. Depth is the distance from the fracture inlet.

dissolution of carbonate minerals predicted by the model probably results from the constrained size of the model domain, which allows the finite amount of initial primary silicate minerals that buffer the low pH in an open CO_2-rich system to be depleted with sufficient CO_2 intrusion. Because the walls of the fracture are thick and new mineral surfaces can be exposed as dissolution occurs, sources of divalent cations are likely to be more stable in actual sequestration reservoirs. However, the models indicate that some reactive minerals can be depleted at the surface, and the remaining Si-rich matrix or secondary precipitation may restrict the accessibility of underlying reactive grains. The difference of accessible reactive surface area depicted by models and the real system is considered a simulation constraint that needs to be amended by the modeler according to the specific system (Pollyea and Rimstidt, 2017).

4.5. Effect of mineral compositions on precipitation

The model provides insight into the source minerals providing divalent cations for carbonate precipitation. The main compositional difference between the flood basalt and the serpentinized basalt is the olivine/serpentine content. Olivine has the fastest dissolution rate among common minerals in basalt. The presence of 9% olivine in the flood basalt allows release of more dissolved Fe^{2+} than from the serpentinized basalt (Fig. 8), enabling more siderite to precipitate in the flood basalt. Olivine and pyroxene are the main sources of divalent cations for carbonation in the flood basalt. In model simulations of the flood basalt reacted at 100 °C and 150 °C, dissolution of olivine and pyroxene leads to depletion of these minerals in the model domain within 40 weeks of reaction (Figs. 14 and 5). This depletion of reactive minerals was not observed in the experiment. Pyroxene and serpentine are the main sources of divalent cations in the serpentinized basalt, and they also dissolve away over 40 weeks (Fig. 16). The plagioclase and the K-rich glass matrix compositions are similarly abundant in flood basalt and serpentinized basalt. While most Ca was supplied by pyroxene, an appreciable amount of plagioclase dissolution provided supplementary Ca over 40 weeks. Previous flow-through experiments on mineral dissolution with the same flood basalt core as in this study revealed that regions of enhanced dissolution along the fracture pathway corresponded to pyroxene and olivine grains(Adeoye et al., 2017).

4.6. Relevance to geologic CO_2 sequestration

This study investigated a far-from-injection-well scenario where most injected CO_2 has already dissolved in groundwater and the CO_2-rich water reacts with basalt containing dead-end microfractures. During the experimental reaction time up to 40 weeks, carbonate precipitates continued to grow on the surface of the fracture without

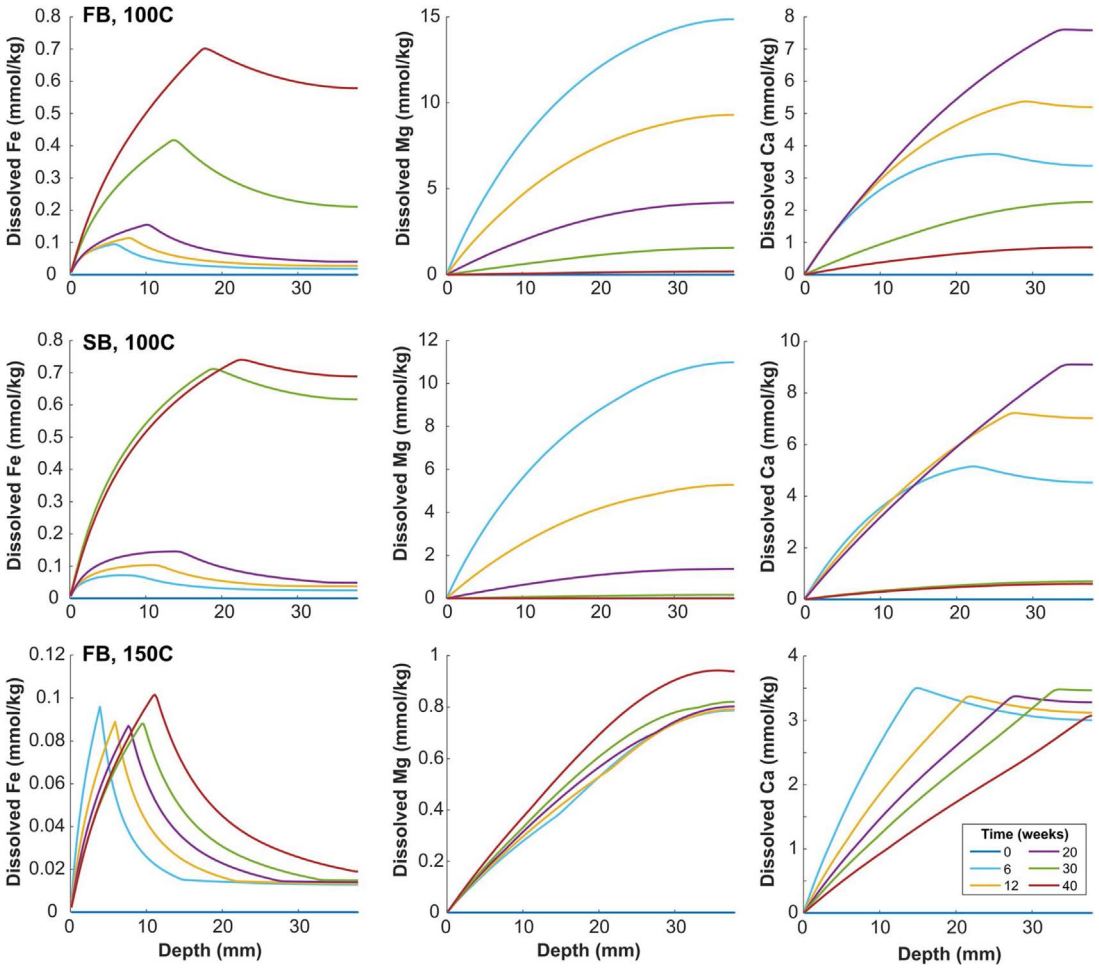

Fig. 10. Predicted dissolved divalent cation concentrations in the fracture domain predicted by the model. The concentrations are zero at 0 mm, where the fracture inlet directly contacts the infinitely diluted bulk solution in the model. Depth is the distance from the fracture inlet.

blocking the transport pathways. In the CarbFix project, the measured divalent cation concentrations continued to decrease one year after injection (Snæbjörnsdóttir et al., 2017), indicating no obvious re-dissolution of carbonate precipitates or reaction zone blockage to cease the entire reaction. Basalt rock surrounding the initial fracture wall continued to dissolve and supply cations to solution. New mineral surfaces can be exposed as dissolution occurs. Carbonate minerals tend to unevenly precipitate on the surface of the basalt fractures in the time scale of months to years; the dissolution/precipitation reactions may reach equilibrium eventually. Unlike the open system in real sites, the fractured basalt in the experiment was a closed system and the bulk solution outside of the fracture could become equilibrated relatively quickly in the experiment. However, over much longer geologic time scales in real reservoirs, the fate of precipitates and the evolution of fractures may vary with the changes in the surrounding environment. The models indicate that some reactive minerals can be depleted at the surface, and the remaining Si-rich matrix or secondary precipitation may restrict the accessibility of underlying reactive grains. Re-dissolution of carbonate precipitates may occur if there is no more reactive mineral supply. Another possibility is that the formation of carbonate minerals in fractures may exert stress on surrounding rocks, creating new fracture surfaces for further reactions; however, fracture cracking was not observed in our experiments.

Overall, the current reactive transport model depicts the chemical gradients along the fracture and reasonably estimates the amount of carbonation despite the limitations. The agreement between the model simulations and experimental observations builds confidence in the model, which can be valuable for using the model to simulate carbon sequestration for a wider range of basalt compositions and reaction conditions than could be studied experimentally.

5. Conclusions

CO_2 mineralization happened rapidly (within 6 weeks) in fractured basalt in this experiment, and complementary reactive transport modeling predicts carbonate formation as early as 1 day. The carbonation products were mainly siderite in this study. The amounts of carbonate minerals formed were different for the two basalts studied. For the more olivine-rich flood basalt, greater volumes of carbonate minerals precipitated and the carbonates that formed were more iron-rich than for the olivine-poor serpentinized basalt. Carbonate minerals were unevenly distributed along microfractures. The zones of maximum carbonate formation did not block the fracture and they did not prevent further mineral trapping reactions in deeper region within the fracture for the conditions of this study.

Acknowledgements

This work was funded by the U.S. Department of Energy (DE-FE0023382). We thank Professor Jill Pasteris for help with Raman spectroscopy and Dr. Hélène Couvy for assistance preparing core samples. Daniel Leib from Musculoskeletal Research Center and Professor James Fitzpatrick from Washington University Center for Cellular Imaging provided support of X-ray computed tomography. Electron microscopy was supported by the Institute of Materials Science and Engineering at Washington University in St. Louis. This study includes

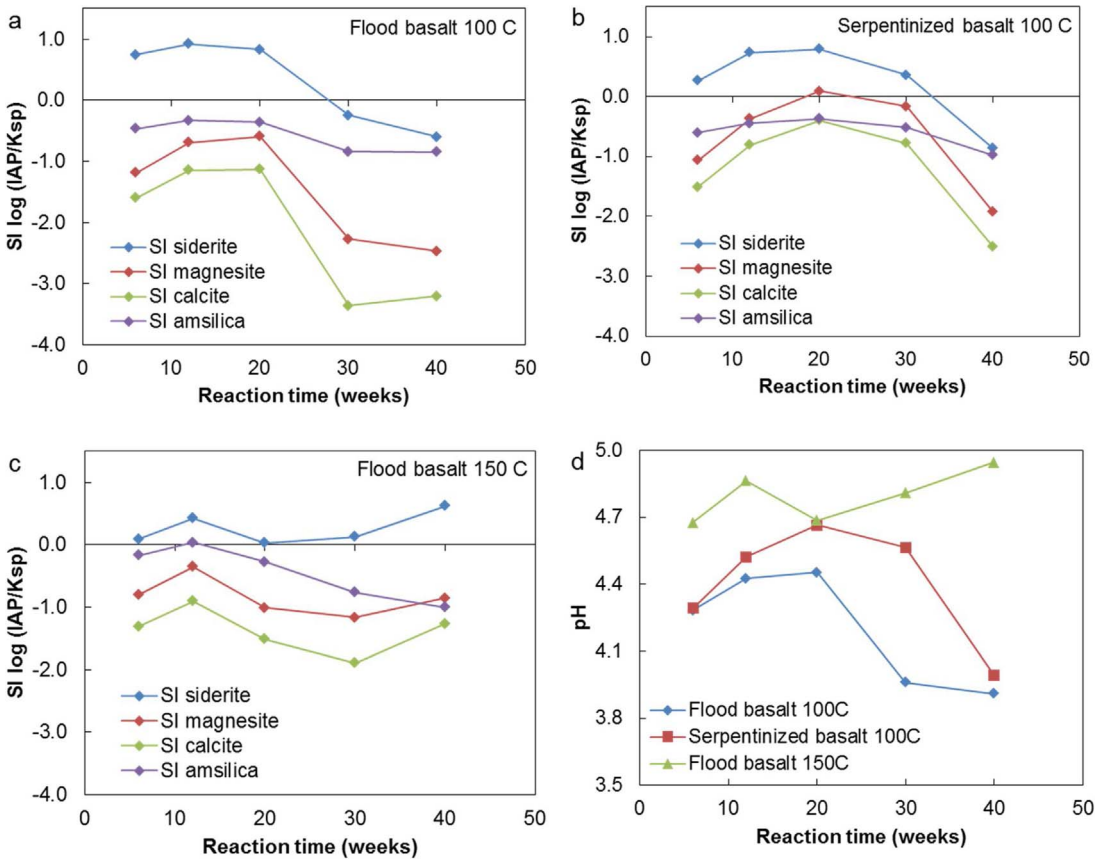

Fig. 11. Saturation indices of the bulk solution outside of the fractured cores after reaction calculated based on measured solute concentrations for a) flood basalt reacted at 100 °C and 10 MPa CO_2; b) serpentinized basalt reacted in 100 °C 10 MPa CO_2; c) flood basalt reacted at 150 °C and 10 MPa CO_2. d) Calculated pH of the bulk solution in three batches; pH calculated based on ion composition at electroneutrality.

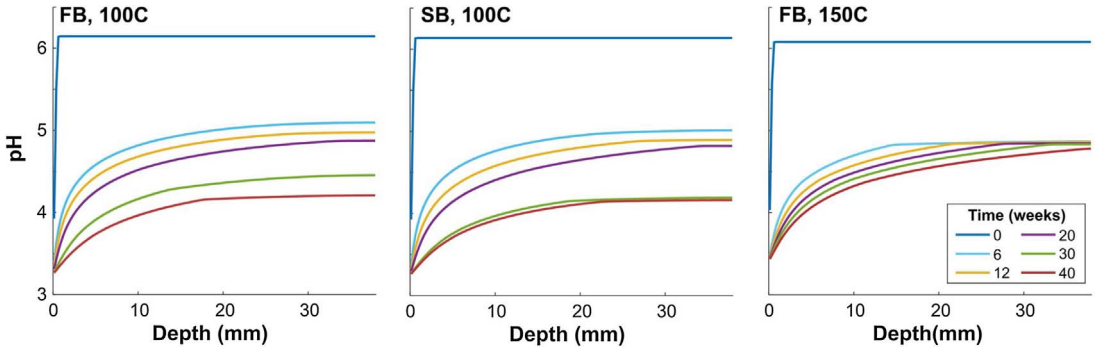

Fig. 12. Calculated pH profiles in the fractures of the cores. Depth is the distance from the fracture inlet.

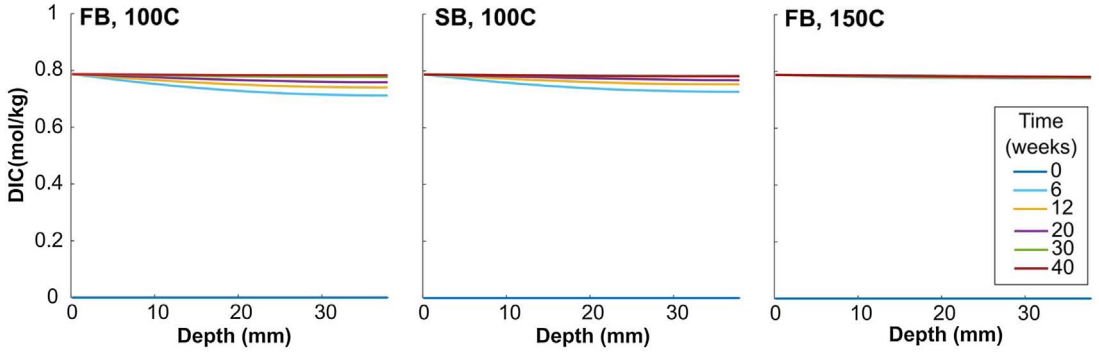

Fig. 13. Dissolved inorganic carbon along the fracture. Depth is the distance from the fracture inlet.

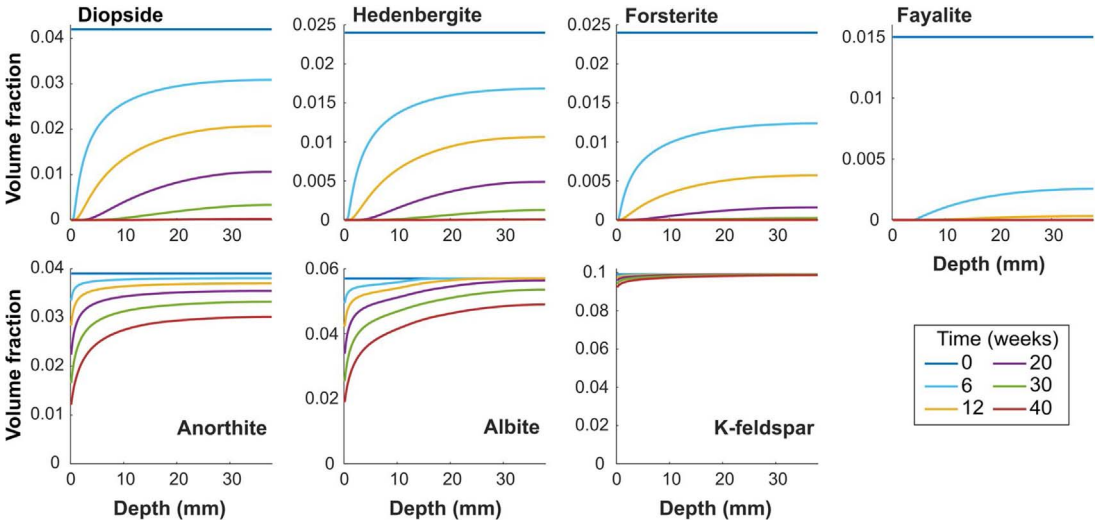

Fig. 14. Predicted amounts of primary minerals in flood basalt during reaction at 100 °C. Amounts of the minerals decrease with time as they dissolve. Depth is the distance from the fracture inlet.

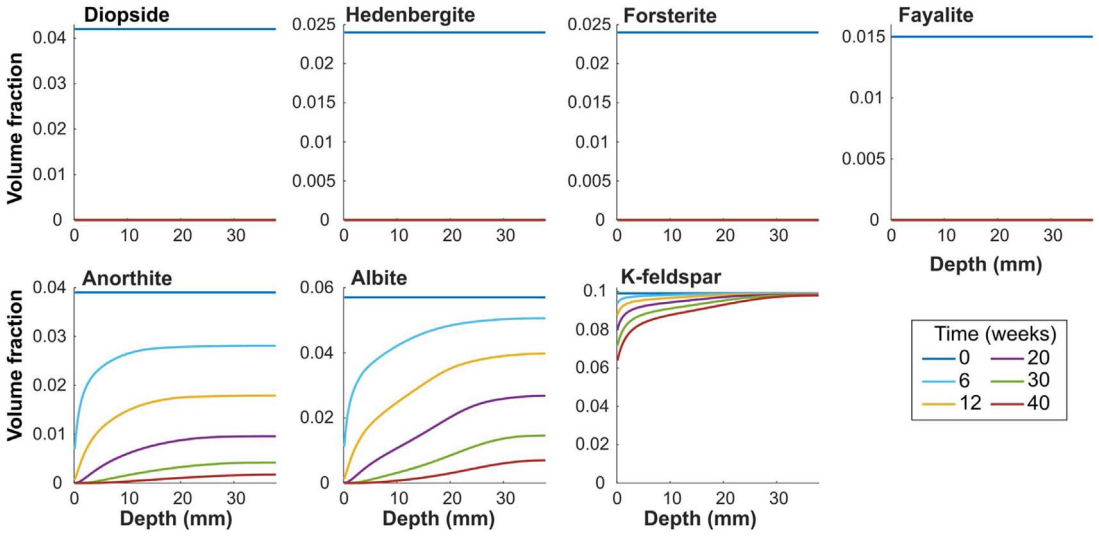

Fig. 15. Predicted amounts of primary minerals in flood basalt during reaction at 150 °C. Amounts of the minerals decrease with time as they dissolve. Depth is the distance from the fracture inlet. Diopside, hedenbergite, forsterite and fayalite dissolve away by 6 weeks.

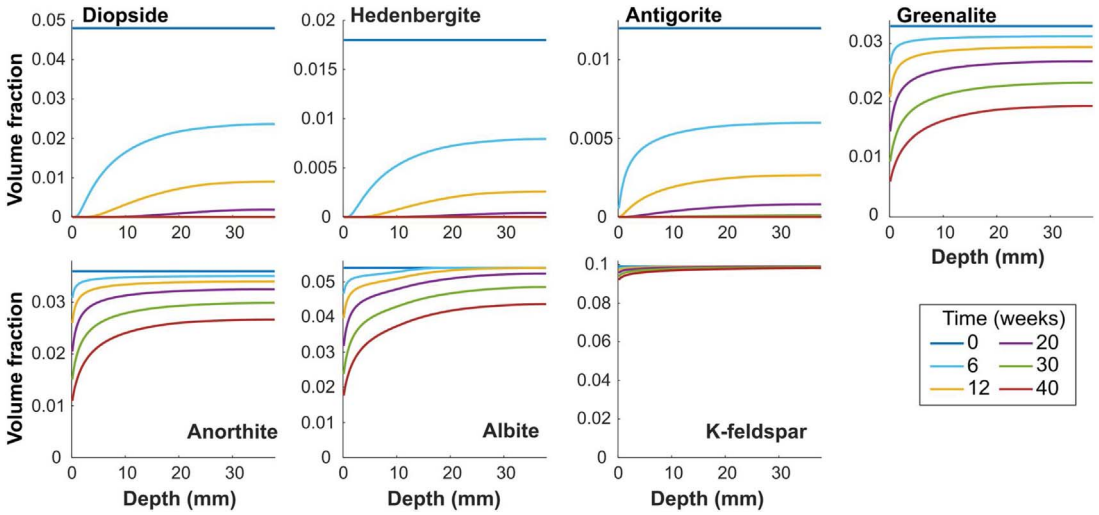

Fig. 16. Predicted amounts of primary minerals in serpentinized basalt during reaction at 100 °C. Amounts of the minerals decrease with time as they dissolve. Depth is the distance from the fracture inlet.

data produced in the CTEES facility at the University of Michigan, supported by the Department of Earth & Environmental Sciences and College of Literature, Science, and the Arts. Jubilee Adeoye assisted with these scans. We appreciate the critical input of Editor Jean-Philippe Nicot, reviewer Ryan Pollyea, and an anonymous reviewer whose comments helped us improve the clarity and technical accuracy of our study.

References

Adeoye, J.T., Menefee, A.H., Xiong, W., Wells, R.K., Skemer, P., Giammar, D.E., Ellis, B.R., 2017. Effect of transport limitations and fluid properties on reaction products in fractures of unaltered and serpentinized basalt exposed to high PCO2 fluids. Int. J. Greenh. Gas Control 63, 310–320.

Aradóttir, E., Sonnenthal, E., Björnsson, G., Jónsson, H., 2012. Multidimensional reactive transport modeling of CO 2 mineral sequestration in basalts at the Hellisheidi geothermal field, Iceland. Int. J. Greenh. Gas Control 9, 24–40.

Benson, S.M., Cole, D.R., 2008. CO_2 sequestration in deep sedimentary formations. Elements 4, 325–331.

Boulard, E., Guyot, F., Fiquet, G., 2012. The influence on Fe content on Raman spectra and unit cell parameters of magnesite–siderite solid solutions. Phys. Chem. Miner. 39, 239–246.

Cadogan, S.P., Maitland, G.C., Trusler, J.M., 2014. Diffusion coefficients of CO_2 and N_2 in water at temperatures between 298.15 K and 423.15 K at pressures up to 45 MPa. J. Chem. Eng. Data 59, 519–525.

Carroll, S.A., McNab, W.W., Dai, Z.R., Torres, S.C., 2013. Reactivity of Mount Simon sandstone and the Eau Claire shale under CO_2 storage conditions. Environ. Sci. Technol. 47, 252–261.

Duan, Z.H., Sun, R., 2003. An improved model calculating CO_2 solubility in pure water and aqueous NaCl solutions from 273 to 533 K and from 0 to 2000 bar. Chem. Geol. 193, 257–271.

Giammar, D.E., Bruant, R.G., Peters, C.A., 2005. Forsterite dissolution and magnesite precipitation at conditions relevant for deep saline aquifer storage and sequestration of carbon dioxide. Chem. Geol. 217, 257–276.

Giammar, D.E., Wang, F., Guo, B., Surface, J.A., Peters, C.A., Conradi, M.S., Hayes, S.E., 2014. Impacts of diffusive transport on carbonate mineral formation from magnesium silicate-CO_2-water reactions. Environ. Sci. Technol. 48, 14344–14351.

Gislason, S.R., Wolff-Boenisch, D., Stefansson, A., Oelkers, E.H., Gunnlaugsson, E., Sigurdardottir, H., Sigfusson, B., Broecker, W.S., Matter, J.M., Stute, M., Axelsson, G., Fridriksson, T., 2010. Mineral sequestration of carbon dioxide in basalt: a pre-injection overview of the CarbFix project. Int. J. Greenh. Gas Control 4, 537–545.

Golubev, S.V., Benezeth, P., Schott, J., Dandurand, J.L., Castillo, A., 2009. Siderite dissolution kinetics in acidic aqueous solutions from 25 to 100 °C and 0–50 atm pCO_2. Chem. Geol. 265, 13–19.

Gysi, A.P., Stefansson, A., 2011. CO_2-water-basalt interaction. Numerical simulation of low temperature CO_2 sequestration into basalts. Geochim. Cosmochim. Acta 75, 4728–4751.

Gysi, A.P., Stefansson, A., 2012. Mineralogical aspects of CO_2 sequestration during hydrothermal basalt alteration – an experimental study at 75–250 °C and elevated pCO_2. Chem. Geol. 306, 146–159.

IPCC, 2005. IPCC Special Report on Carbon Dioxide Capture and Storage. Cambridge University Press for the Intergovernmental Panel on Climate Change, Cambridge.

Kaiser, K., Guggenberger, G., 2003. Mineral surfaces and soil organic matter. Eur. J. Soil Sci. 54, 219–236.

Kelemen, P.B., Matter, J., 2008. In situ carbonation of peridotite for CO_2 storage. Proc. Natl. Acad. Sci. U. S. A. 105, 17295–17300.

Kintisch, E., 2016. New solution to carbon pollution? Science 352, 1262–1263.

Knauss, K.G., Johnson, J.W., Steefel, C.I., 2005. Evaluation of the impact of CO_2, co-contaminant gas, aqueous fluid and reservoir rock interactions on the geologic sequestration of CO_2. Chem. Geol. 217, 339–350.

Luhmann, A.J., Tutolo, B.M., Tan, C.Y., Moskowitz, B.M., Saar, M.O., Seyfried, W.E., 2017. Whole rock basalt alteration from CO_2-rich brine during flow-through experiments at 150 °C and 150 bar. Chem. Geol. 453, 92–110.

Matter, J.M., Kelemen, P.B., 2009. Permanent storage of carbon dioxide in geological reservoirs by mineral carbonation. Nat. Geosci. 2, 837–841.

Matter, J.M., Stute, M., Snaebjornsdottir, S.O., Oelkers, E.H., Gislason, S.R., Aradottir, E.S., Sigfusson, B., Gunnarsson, I., Sigurdardottir, H., Gunnlaugsson, E., Axelsson, G., Alfredsson, H.A., Wolff-Boenisch, D., Mesfin, K., Taya, D.F.D., Hall, J., Dideriksen, K., Broecker, W.S., 2016. Rapid carbon mineralization for permanent disposal of anthropogenic carbon dioxide emissions. Science 352, 1312–1314.

McGrail, B.P., Schaef, H.T., Spane, F.A., Cliff, J.B., Qafoku, O., Horner, J.A., Thompson, C.J., Owen, A.T., Sullivan, C.E., 2017. Field validation of supercritical CO_2 reactivity with basalts. Environ. Sci. Technol. Lett. 4, 6–10.

Menefee, A.H., Li, P., Giammar, D.E., Ellis, B.R., 2017. Roles of transport limitations and mineral heterogeneity in carbonation of fractured basalts. Environ. Sci. Technol. 51, 9352–9362.

Oelkers, E.H., Gislason, S.R., Matter, J., 2008. Mineral carbonation of CO_2. Elements 4, 333–337.

Orlando, A., Borrini, D., Marini, L., 2011. Dissolution and carbonation of a serpentinite: inferences from acid attack and high P-T experiments performed in aqueous solutions at variable salinity. Appl. Geochem. 26, 1569–1583.

Palandri, J.L., Kharaka, Y.K., 2004. A compilation of rate parameters of water-mineral interaction kinetics for application to geochemical modeling. DTIC Document.

Pokrovsky, O.S., Schott, J., 2002. Surface chemistry and dissolution kinetics of divalent metal carbonates. Environ. Sci. Technol. 36, 426–432.

Pokrovsky, O.S., Golubev, S.V., Schott, J., 2005. Dissolution kinetics of calcite, dolomite and magnesite at 25 °C and 0–50 atm pCO_2. Chem. Geol. 217, 239–255.

Pollyea, R.M., Rimstidt, J.D., 2017. Rate equations for modeling carbon dioxide sequestration in basalt. Appl. Geochem. 81, 53–62.

Schaef, H.T., McGrail, B.P., Owen, A.T., 2010. Carbonate mineralization of volcanic province basalts. Int. J. Greenh. Gas Control 4, 249–261.

Schaef, H.T., McGrail, B.P., Owen, A.T., 2011. Basalt reactivity variability with reservoir depth in supercritical CO_2 and aqueous phases. Energy Procedia 4, 4977–4984.

Schneider, C.A., Rasband, W.S., Eliceiri, K.W., 2012. NIH Image to ImageJ: 25 years of image analysis. Nat. Methods 9, 671–675.

Schrag, D.P., 2007. Preparing to capture carbon. Science 315, 812–813.

Sissmann, O., Brunet, F., Martinez, I., Guyot, F., Verlaguet, A., Pinquier, Y., Daval, D., 2014. Enhanced olivine carbonation within a basalt as compared to single-phase experiments: reevaluating the potential of CO_2 mineral sequestration. Environ. Sci. Technol. 48, 5512–5519.

Snæbjörnsdóttir, S.Ó., Oelkers, E.H., Mesfin, K., Aradóttir, E.S., Dideriksen, K., Gunnarsson, I., Gunnlaugsson, E., Matter, J.M., Stute, M., Gislason, S.R., 2017. The chemistry and saturation states of subsurface fluids during the in situ mineralisation of CO_2 and H_2S at the CarbFix site in SW-Iceland. Int. J. Greenh. Gas Control 58, 87–102.

Sommer, C., Straehle, C., Koethe, U., Hamprecht, F.A., 2011. Ilastik: interactive learning and segmentation toolkit. 2011 IEEE International Symposium on Biomedical Imaging: From Nano to Macro. IEEE 230–233.

Steefel, C.I., Appelo, C.A.J., Arora, B., Jacques, D., Kalbacher, T., Kolditz, O., Lagneau, V., Lichtner, P.C., Mayer, K.U., Meeussen, J.C.L., Molins, S., Moulton, D., Shao, H., Simunek, J., Spycher, N., Yabusaki, S.B., Yeh, G.T., 2015. Reactive transport codes for subsurface environmental simulation. Comput. Geosci. 19, 445–478.

Teir, S., Revitzer, H., Eloneva, S., Fogelholm, C.J., Zevenhoven, R., 2007. Dissolution of natural serpentinite in mineral and organic acids. Int. J. Miner. Process. 83, 36–46.

Tester, J.W., Worley, W.G., Robinson, B.A., Grigsby, C.O., Feerer, J.L., 1994. Correlating quartz dissolution kinetics in pure water from 25 °C to 625 °C. Geochim. Cosmochim. Acta 58, 2407–2420.

Thevenaz, P., Ruttimann, U.E., Unser, M., 1998. A pyramid approach to subpixel registration based on intensity. IEEE Trans. Image Process. 7, 27–41.

Wells, R.K., Xiong, W., Sesti, E., Cui, J., Giammar, D., Skemer, P., Hayes, S.E., Conradi, M.S., 2017. Spatially-variable carbonation reactions in polycrystalline olivine. Geochim. Cosmochim. Acta 204, 252–266.

Xiong, W., Giammar, D., 2014. Forsterite carbonation in zones with transport limited by diffusion. Environ. Sci. Technol. Lett. 1, 333–338.

Xiong, W., Wells, R.K., Giammar, D.E., 2017. Carbon sequestration in olivine and basalt powder packed beds. Environ. Sci. Technol. 51, 2105–2112.

Zhang, S., DePaolo, D.J., Xu, T., Zheng, L., 2013. Mineralization of carbon dioxide sequestered in volcanogenic sandstone reservoir rocks. Int. J. Greenh. Gas Control 18, 315–328.